Thermal transport across nanoparticle–fluid interfaces: the interplay of interfacial curvature and nanoparticle–fluid interactions

Thermal transport across nanoparticle-fluid interfaces: the interplay of interfacial curvature and nanoparticle-fluid interactions †

Anna Sofia Tascini[a], Jeff Armstrong[a,b], Eliodoro Chiavazzo[c], Matteo Fasano[c], Pietro Asinari[c] and Fernando Bresme[*,a]

We investigate the general dependence of the thermal transport across nanoparticle-fluid interfaces using molecular dynamics computations. We show that the thermal conductance depends strongly both on the wetting characteristics of the nanoparticle-fluid interface as well as on the nanoparticle size. Strong nanoparticle-fluid interactions, leading to full wetting states in the host fluid, result in high thermal conductances and efficient interfacial transport of heat. Weak interactions result in partial drying or full drying states and low thermal conductances. The variation of the thermal conductance with particle size is found to depend on the fluid-nanoparticle interactions. Strong interactions coupled with large interfacial curvatures lead to optimum interfacial heat transport. This complex dependence can be modelled with an equation that includes the interfacial curvature as parameter. In this way we rationalise existing experimental and computer simulation results and show that the thermal transport across nanoscale interfaces is determined by the correlations of both interfacial curvature and nanoparticle-fluid interactions.

1 Introduction

Nanoparticles offer numerous opportunities in technological applications[1], analytical chemistry[2] and medicine[3]. They can be coated with a wide range of ligands, which provide specific functionality in catalysis[4,5], or define the mechanical response of nanoparticle arrays[6].

Nanoparticles are of current interest in applications concerned with thermal transport. Metal nanoparticles and metal nanostructures can be used as nanoheaters that convert light into heat. This property is being exploited to set up nanoscale mass fluxes[7,8] and in thermal therapy applications, where the nanoparticles can bind specifically to cells. It has been shown that the temperature next to the particle can increase by hundreds of degrees, resulting in the explosive evaporation of the fluid, a phenomenon that takes place in subnanosecond timescales[9]. Magnetic particles containing iron oxide cores are also of interest in the area of thermal therapies as they can be heated by applying magnetic fields[10]. The description of heat flow from the nanoparticles to the surrounding fluid is challenging and it involves the full complexity of thermal transport at the nanoscale[11,12]. Indeed, the heat transport is expected to be strongly influenced by the interfacial properties: surface free energies, interfacial curvature and interfacial structure. As a matter of fact there is evidence that nanoparticles influence the diffusion of water at the nanoparticle-water interface (see *e.g.* [13]). Advancing in the development of technological applications involving nanoparticle heating requires a good understanding of the mechanisms that determine and control the transport of heat from the particle to the surrounding medium. This problem inevitably involves the investigation of thermal transport through the nanoparticle-fluid interface, and the quantification of the interfacial thermal conductance. The latter determines the temperature increase of the surrounding fluid as well as the characteristic time scale of the temperature relaxation towards the equilibrium temperature. Hence, the quantification of the thermal conductance of nanoparticle-fluid interface is a problem of evident practical significance.

Thermoreflectance experiments of monolayers adsorbed on solid substrates have shown that the thermal conductance depends significantly on chemical composition[14,15]. These studies show that hydrophilic interfaces (alkane layers with polar terminal groups) feature higher thermal conductances, ~ 150 MW/(m^2 K), than hydrophobic interfaces (alkane layers with methyl terminal groups), ~ 50 MW/(m^2 K). Molecular dynamics simulations have confirmed this dependence, and predicted thermal conductance in quantitative agreement with the experimental data[16]. Recent studies on flat surfaces, have suggested that the thermal

[a] *Department of Chemistry, Imperial College London, SW7 2AZ, UK Email:anna.tascini13@imperial.ac.uk;f.bresme@imperial.ac.uk*

[b] *ISIS Facility, Rutherford Appleton Laboratory, Chilton, Didcot, Oxfordshire, OX11 0QX, UK*

[c] *Department of Energy, Politecnico di Torino, 10129, Torino, Italy*

† Electronic supplementary information (ESI) available. See DOI: 10.1039/c6cp06403e

conductance varies linearly with the work of adhesion of the surface[17]. Such a correlation might be useful to predict heat transport in nanoparticle-fluid interfaces. This is a significant objective given the difficulty associated with experimental measurements at the nanoscale. However, the generality of such correlations has not been established yet, and their applicability to nanoparticles remains an outstanding question.

Recently, our group considered the impact of curvature on thermal conductance[18]. This study was performed using transient non-equilibrium molecular dynamics simulations of alkane nanoparticles immersed in water. It was found that the thermal conductance can be high and of the order of that found in hydrophilic surfaces. It was further shown that this surprising result is a consequence of the strong dependence of the thermal conductance with nanoparticle curvature. An extrapolation of the thermal conductances to those of a flat wall (zero curvature) predicted much lower conductances, with values in agreement with those reported for flat hydrophobic interfaces[14,17,18]. More recently, the dependence of the thermal conductance with curvature has been confirmed in simulation studies of metal oxide nanoparticles immersed in octane[19], and in theoretical studies of nano-bubbles and nanodroplets[20,21]. Computer simulations have further highlighted the importance of intermolecular interactions and interface structure on thermal conductance[22–25], and the relevance of interfacial curvature on vapour nucleation around nanoparticles[26].

The above discussion summarizes our current understanding of thermal transport in nanoparticle-fluid interfaces. Both experimental and theoretical studies have identified the interfacial composition as a key variable in interfacial thermal transport of flat surfaces. However, the experimental data for nanoparticles are still scarce and the estimates of the thermal conductance involve significant uncertainties. Overall, a good understanding on how the thermal conductance depends both on interface curvature and fluid-nanoparticle interaction is still lacking. We have thus undertaken an investigation using molecular dynamics simulations in combination with generic nanoparticle models, which allow us to uncover the key correlations between nanoparticle curvature and nanoparticle-fluid interactions, and also how these correlations define the thermal conductance of nanoparticle-fluid interfaces.

Our paper is structured as follows. We describe first the simulation models and our computational approach to study heat transport across nanoparticle-fluid interfaces. A discussion of our main results on the dependence of the thermal conductance of the nanoparticle-fluid interface with different wetting characteristics and nanoparticle curvature follows. We then discuss the implications of our results for the interpretation of existing experimental and simulation data of thermal conductances. We close the paper with a final section devoted to our main conclusions and final remarks.

2 Methods

2.1 Nanoparticle models

We have chosen for our study a generic model of a nanoparticle immersed in a fluid (see Fig. 1). The model allows a systematic investigation of the variation of the interfacial thermal conductance with the nanoparticle diameter and nanoparticle-fluid (NP-f) interactions. Nanoparticles of different diameters were built by cutting a sphere from a FCC solid, by selecting all the atoms inside a sphere of a given radius. The lattice constant of the solid, l_c, was defined by $l_c = (4/\rho_{NP})^{1/3}$, with the density set to $\rho^*_{NP} = \rho_{NP}\sigma^3 = 1$, σ being the atomic diameter. We employ throughout this work Lennard-Jones reduced units to represent our results. All the properties given in these units are denoted with the superscript "*". In order to evaluate the dependence of the thermal conductance with the nanoparticle curvature, we studied different nanoparticle radii, $R^* = R/\sigma$=5, 6, 7, 8 and 10 ($\sim$ 1.5-3.5 nm for atom diameters of the order of the gold atom). The particle was immersed in a Lennard-Jones fluid, where the positions of the atoms were set randomly. A typical simulation consisted of $N \sim 2\times10^4 - 10^5$ particles in a cubic simulation box with box length L*=30–50, depending on the nanoparticle diameter. Periodic boundary conditions were applied in all directions.

The fluid was modelled with the Lennard-Jones (LJ) potential, and the density was set to $\rho^*_L = \rho_L\sigma^3 = 0.8$, which is close to the density of the Lennard-Jones fluid at triple point conditions[27]. The atoms in the fluid and the nanoparticle had the same diameter, σ.

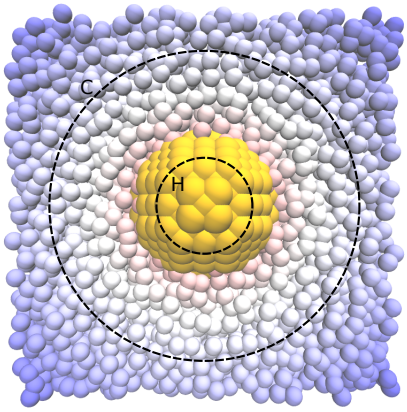

Fig. 1 Snapshot of a representative configuration of a nanoparticle (yellow) of radius $R^* = 5$ immersed in the fluid (white-blue). The dashed circles represent the boundaries of the hot (H, inner circle) and cold (C, outer circle) thermostats.

The nanoparticle-nanoparticle and fluid-fluid interactions were truncated at a cut-off $r^*_c = 2.5$. Employing a different cut-off results in slightly different coexistence properties and transport coefficients, but it does not affect the general physical behaviour reported in our work. We have performed new simulations with a longer cut-off, $r^*_c = 4.4$ and we find the temperature profiles are very similar to those calculated with the shorter cut-off (see Fig. S1 in the ESI†). Hence we chose $r^*_c = 2.5$ for our simulations, as it offers a good compromise between accuracy and speed of computation. The interatomic interactions between atoms were set to $\frac{\varepsilon_{NP}}{\varepsilon_f} = 10$, where ε_{NP} and $\varepsilon_f = 1$ are the interaction strength between atoms in the nanoparticle and in the fluid, respectively. The interaction strength for the NP is similar to the one employed in LJ models of metals[28]. To investigate the dependence of the in-

terfacial conductance with nanoparticle wettability we varied the nanoparticle-fluid interaction using $\varepsilon_{NP-f} = F\sqrt{\varepsilon_{NP}\,\varepsilon_f}$. By tuning the parameter F, we were able to model different wetting states, from full drying to full wetting. We quantified the wetting state by computing the contact angle of the nanoparticle with the liquid-vapour interface. This calculation should provide a link with experimental studies, which now allow the direct measurements of contact angles of very small nanoparticles [29].

2.2 Non-Equilibrium molecular dynamics

A temperature gradient was imposed through the nanoparticle-fluid interface using Boundary Driven Non-Equilibrium Molecular Dynamics (NEMD) simulations. The thermostats were set up by defining two regions. The hot thermostat was set as a spherical volume of radius $r_H^* = R^* - 2$, located at the center of the nanoparticle. The cold thermostat was defined by the region between a spherical surface at $r_C^* = R^* + 7$ and the edge of the simulation box (see Fig. 1).The shell thickness for the cold layer was equal to 3 (in LJ units) for all the simulations. The location of the thermostats does not influence the thermal conductances reported in this work. All the atoms in the nanoparticle were tethered to their original positions (at the start of the simulation) using a harmonic potential with a force constant, $k^* = 100$. This harmonic potential prevented nanoparticle drifts during the simulation.

The NEMD simulations were implemented as follows. Firstly, we performed canonical simulations using the Nosé-Hoover thermostat with a damping parameter of $\tau^* = 0.2$. These simulations involved 10^6 steps. The equations of motion were integrated using the velocity-Verlet algorithm and the code LAMMPS [30] using $\delta t^* = 0.001$ for the integration timestep. The temperature of the simulation, $T^* = 0.72$, is above the triple point temperature of our LJ model [31]. We selected this temperature to generate the liquid-vapour interface that was used to quantify the wettability of the nanoparticle (see below).

Following the equilibration period, the thermostats were set at the temperatures $T_{HOT}^* = 0.92$ and $T_{COLD}^* = 0.72$, by rescaling the velocities of the atoms inside those regions at every timestep. Following the rescaling, we reset the linear momentum of the entire simulation box to zero. To ensure the systems used in the analyses had reached the stationary state, we discarded the first 5×10^5 timesteps. The production stage involved typically 5×10^6 timesteps, and it was used to compute the average properties reported below. All the errors reported in this work are given as one standard deviation of the mean and were obtained from the analysis of ten consecutive trajectories of 5×10^5 timesteps each.

2.3 Temperature profile and heat flux evaluation

To obtain spatial averages the system was subdivided into $70-125$ (depending on system size) spherical shells of thickness $\delta r^* = 0.2$, centered around the centre of mass of the nanoparticle. The local temperature was computed using the equipartition formula, $T(r) = \sum_{i=1}^{N\in r} m_i v_i^2/(k_B N_f)$, where the sum runs over all the particles located in a shell with radius r, and N_f represents the number of degrees of freedom. We show in Fig. 2 a representative temperature profile along the radial distance to the center of the nanoparticle. The temperature profile shows a clear discontinuity at the nanoparticle-fluid interface, $r^* = 5$, which is connected to the interfacial thermal conductance, G_K.

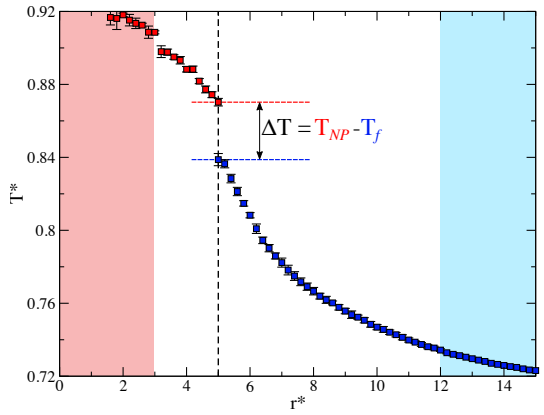

Fig. 2 Representative temperature profile (red squares – nanoparticle, blue squares – fluid) along the radial distance from the centre of mass of a nanoparticle of radius $R^* = 5$ in a simulation box of length, $L_x^* = L_y^* = L_z^* = 30$. The coloured regions, red and blue, represent the location of the thermostats, hot and cold, respectively.

We evaluated the thermal conductance from

$$G_K = \frac{J_q}{\Delta T}, \tag{1}$$

where $\Delta T = T_{NP} - T_f$ represents the temperature "jump" at nanoparticle (T_{NP})-fluid (T_f) interface (see Fig. 2), and J_q is the heat flux at the radius where we observe the temperature jump. The temperature profile in the fluid phase can be fitted to the Fourier's law result, which at the steady state, is given by [32] $T(r) = A/r + B$, where A and B are constants that can be estimated by considering the boundary conditions of the heat diffusion equation (see ESI†).

The heat flux is a key quantity in the computation of the interfacial thermal conductance. It can be obtained from the continuity equation,

$$J_q = \frac{\langle \Delta U \rangle}{A(r)\delta t}, \tag{2}$$

where $A(r) = 4\pi r^2$ is the area of a spherical surface of radius r, and $\langle \Delta U \rangle$ is the time average of the change in the internal energy associated with the thermostatting process in the hot or cold regions. The velocity rescaling is performed without modifying the particle coordinates, hence $\Delta U(t) = K_{new}(t) - K_{old}(t)$ at time t is obtained every timestep by calculating the difference between the kinetic energies after, K_{new}, and before, K_{old}, the rescaling.

The heat flux was computed using the statistical mechanics equation derived by Irving and Kirkwood [33]:

$$J_U(V) = \frac{1}{V}\sum_{i=1}^{N\in V}\left[\frac{1}{2}m_i\mathbf{v}_i^2\mathbf{v}_i + \phi_i\mathbf{v}_i + \frac{1}{2}\sum_{j\neq i}\left(\mathbf{v}_i\cdot\mathbf{F}_{ij}\right)\mathbf{r}_{ij}\right], \tag{3}$$

where the sum runs over all the particles inside the control volume, V. This volume is defined by a spherical shell of radius r and thickness 0.2. m_i and $\mathbf{v}_i$ represent the mass and velocity of particle i, respectively, ϕ_i, is the potential energy of particle i, $\mathbf{F}_{ij}$

the force of particle j on i, and $\mathbf{r}_{ij} = \mathbf{r}_i - \mathbf{r}_j$.

The consistency between eqn (2) and (3) has been explored before for charged and polar fluids[34–36]. We find that these approaches are also consistent in the case of the spherical geometry considered here (see Fig. 3).

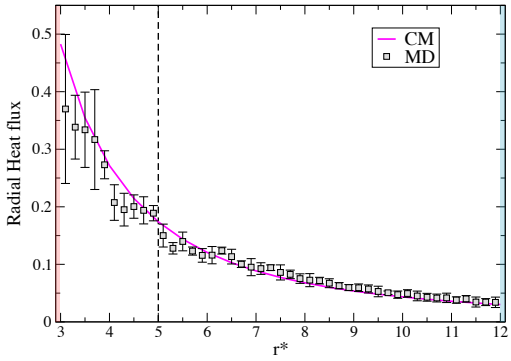

Fig. 3 Radial heat flux for a nanoparticle of radius, $R^* = 5$. The full line (CM) represents the heat flux obtained from the continuity equation, eqn (2) and the symbols (MD) the internal energy flux from the molecular dynamics simulations and eqn (3).

3 Results and Discussion

3.1 Nanoparticle wettability

In preparation for the analysis of the thermal conductance, we performed equilibrium simulations of the nanoparticle-liquid-vapour contact angles. We show in Fig. 4, a snapshot illustrating the simulation set up, consisting of one nanoparticle adsorbed at the liquid-vapour interface at $T^* = 0.72$, with coexisting densities, $\rho_l^* = 0.77$ and $\rho_v^* = 0.009$ for the liquid and vapour phases, respectively. These densities are in good agreement with previous molecular dynamics simulations of the same LJ model[31]. The density profiles were obtained from an analysis over 2000 configurations. The contact angle was estimated following the approaches discussed in a previous work[37]. We show in Fig. 4 the dependence of the contact angle with the interaction parameter, F. Partial wetting or drying states are defined by values in the range $0.05 < F < 0.25$. Interaction strengths outside this range correspond to either dry or wet states. We will discuss below the thermal conductance with reference to the wetting states obtained here.

3.2 Temperature profiles around nanoparticles

We show in Fig. 5 the temperature profiles for a nanoparticle of radius $R^* = 5$ as a function of the fluid-particle interaction strength, F. The thermal gradients in the nanoparticle and fluid regions are determined by the different heat fluxes employed in the simulations and the different nanoparticle and fluid thermal conductivities. We report numerical data for the thermal conductivities extracted from the analysis of the profiles in Tables S1 and S2 in the ESI† . The thermal conductivities of the nanoparticle are of the order of the ones reported before for bulk solids[38]. We also observe a slight increase in the thermal conductivity with interaction strength (see Table S1 and Fig. S2 in the ESI†), which we

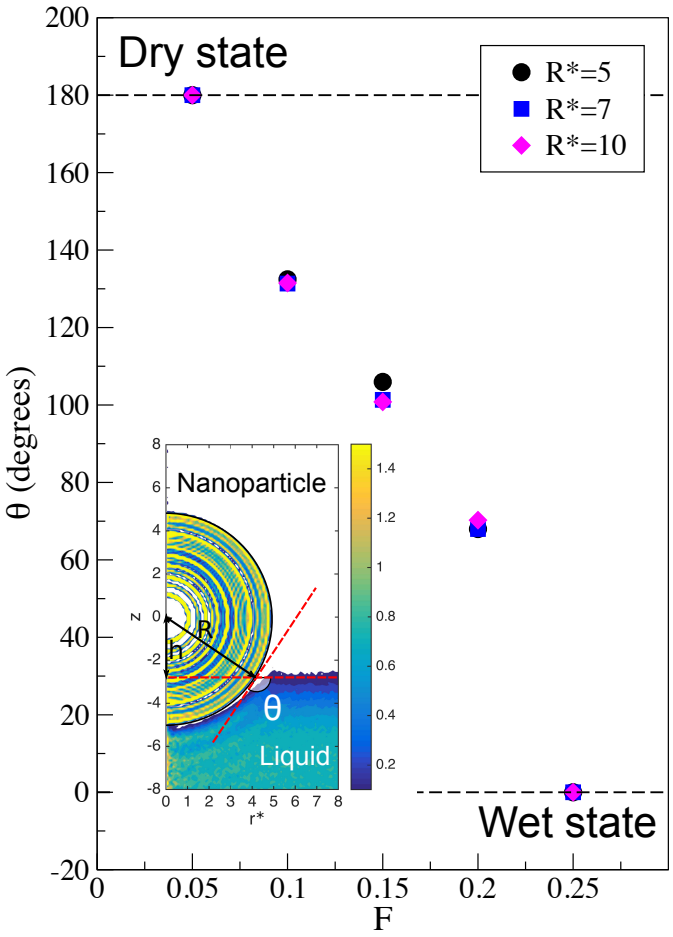

Fig. 4 Dependence of the nanoparticle contact angle with the interaction parameter F for different particle radii $R^* = 5, 7$ and 10. (Inset) Average density profile of the nanoparticle and the liquid-vapour interface. The definition of the contact angle, θ, in terms of the immersion h and particle radius, R, is also shown. The contact angle is given by $\cos\theta = h/R$. The colour map indicates different densities, ρ^* (see vertical bar for numerical values of the density).

associate to the strong adsorption of the fluid on the nanoparticle in the wetting regime F>0.25. The temperature profile around the nanoparticle features the characteristic temperature "jump", which can be used to quantify the thermal conductance of the nanoparticle-fluid interface. The magnitude of the temperature jump varies significantly with the nanoparticle-fluid interaction, F, decreasing as F increases, *i.e.*, stronger fluid-nanoparticle interactions result in interfaces that are better heat conductors.

We have fitted our simulated temperature profiles to the solution of the one dimensional heat diffusion equation under stationary conditions[32] (see ESI† for detailed information). Fig. 5 shows both the simulation and the continuum model fitting. The continuum model is satisfactory, showing that the approximation of constant thermal conductivities that we have adopted for the nanoparticle and the fluid are reasonable for the temperature range considered here. We compile in the ESI† (Tables S1 and S2) numerical data for the thermal conductance. These data show that the estimates of the thermal conductance obtained from the

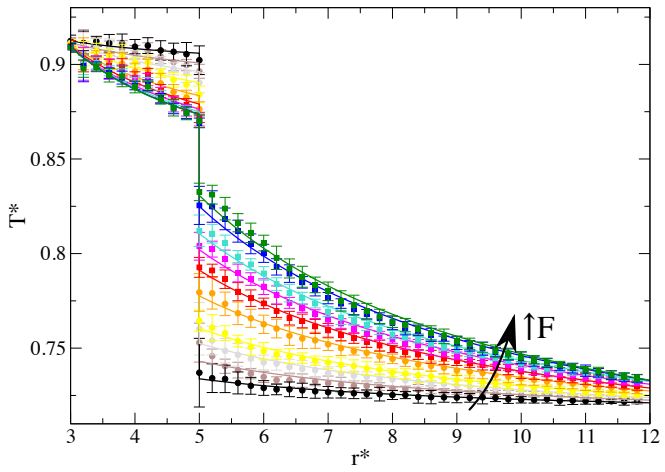

Fig. 5 Temperature profiles as a function of the interaction strength, from F=0.05 (black curve - bottom fluid region) to F=1.0 (green curve - top fluid region) (see arrow in the plot and Table S1 in the ESI† for a list of the different values for F). Squares and circles represent systems with $\varepsilon_{NP} > \varepsilon_f$ and $\varepsilon_{NP} < \varepsilon_f$, respectively. The lines correspond to the solutions of the heat diffusion equation using the finite difference method discussed in the ESI†. The results correspond to a nanoparticle of radius $R^* = 5$.

heat diffusion equation solution and the direct calculation of the temperature "jump" are consistent with each other.

3.3 Thermal conductance

We show in Fig. 6 the thermal conductance computed from eqn (1) as a function of the nanoparticle-fluid interaction strength. We employed in our computation the temperatures at both sides of the temperature "jump", which is located at the particle surface, R^* (see Fig. 5). The "jump" is very well defined in all our systems and the thermal conductance can be determined accurately. The thermal conductances feature a strong dependence on the interaction strength, F. We find no distinctive discontinuous changes in G_K at the drying, F=0.05, or wetting, F=0.25, transitions. The extrapolation of the thermal conductances to F$\to$ 0 indicates that the resulting interface has a very low thermal conductance, $G_k = 0.017 \pm 0.007$, which corresponds to ~ 0.939 MW/(K m^2) in SI units. This thermal conductance is similar to the values reported for liquid-vapour interfaces[39] and is consistent with the fact that at F=0 our system is in the drying region and the nanoparticle would be surrounded by a vapour layer. This result supports the validity of our model in predicting thermal conductances that are consistent with existing results.

Computer simulations of self assembled monolayers in contact with water[17] indicate that the thermal conductance varies linearly with the wetting characteristics of the surface. This dependence follows from an analysis of the work of adhesion required to separate water from the monolayer. For nanoparticles the analysis of the correlation between the work of adhesion and the nanoparticle wetting properties is much more complex, since we need to quantify the free energy of nanoparticle adsorption at the liquid-vapour interface. For spherical particles, this free energy can be written as[37]

$$\mathscr{F} = (\gamma_{p2} - \gamma_{p1})A_{p2} - \gamma_{12}A_{st}, \tag{4}$$

where $\gamma_{p\alpha}$ is the interfacial tension of the nanoparticle with phase α, either liquid or vapour, γ_{12} is the liquid-vapour surface tension, A_{p2} the area of the nanoparticle in contact with phase 2, and A_{st} the cross sectional area of interface "12" removed by the nanoparticle. In eqn (4) we have assumed that the line tension effects can be neglected. This notion is consistent with computations of LJ nanoparticles adsorbed at liquid-vapour interfaces. These studies showed that the line tension has a small effect on the particle wettability for nanoparticle radii $R^* \geq 5$[37,40]. Following Aveyard and Clint[41] eqn (4) can be re-written as:

$$\bar{\mathscr{F}} = -\frac{1}{4}(1-\bar{h}^2) + \frac{1}{2}\cos\theta(1-\bar{h}), \tag{5}$$

where $\bar{\mathscr{F}} = \mathscr{F}/(\gamma_{12}A_p)$, $A_p = 4\pi R^2$ is the total area of the spherical particle with radius R, and $\bar{h} = h/R$ quantifies the nanoparticle immersion. When the centre of mass of the particle is located at the interface $\theta = \pi/2$ and $h = 0$.

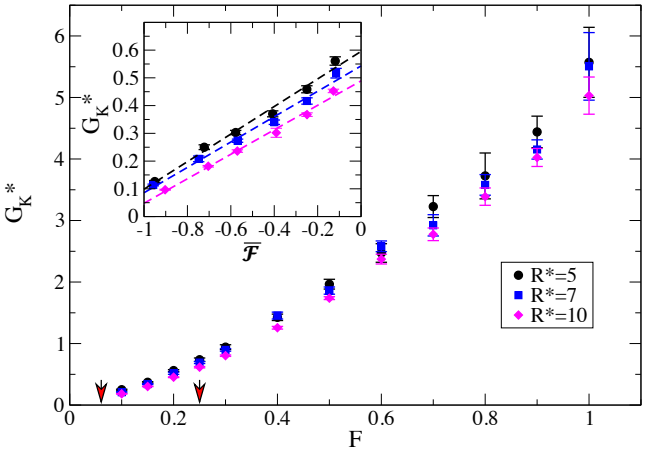

Fig. 6 Dependence of the thermal conductance with the interaction strength, F, and the nanoparticle radius. The red arrows on the x-axis indicate the drying (F=0.05) and wetting (F=0.25) transitions. (Inset) Dependence of the thermal conductance on the free energy of adsorption, $\bar{\mathscr{F}}$, for thermodynamic states in the partial wetting regime, *i.e.*, between the arrows in the main plot. The different lines and symbols represent the results for different particle radii. The colours have the same meaning as in the main plot.

We have investigated the dependence of the thermal conductance on the free energy of adhesion of the nanoparticle with the fluid, $\bar{\mathscr{F}}$ (see eqn (5) and inset in Fig. 6). We find that G_K varies linearly with the nanoparticle work of adhesion for the different nanoparticle radii. The linear dependence is consistent with the trends observed in reference[17] for liquid-monolayer interfaces, and it is remarkable that a similar trend is observed in the case of nanoparticles when the appropriate adsorption energy (eqn (5)) is considered. A linear regression to $G_K^* = a + b\bar{\mathscr{F}}$ using all the

particle sizes, gives a slope of $b \sim 0.5$. This value corresponds in real units to 28 MW/(K m^2) (using Lennard-Jones units for argon, $\sigma = 0.3405$ nm, ε =1 kJ/mol and m=39.94 g/mol). The estimated slope for self assembled monolayers in contact with water is 85 MW/(m^2 K) [17]. These results show the difficulty in mapping different substrates (surfaces, nanoparticles) and fluids to a general master curve that would relate the thermal conductance to the work of adhesion. Indeed, our own data reveal deviations across systems, which correlate with nanoparticle size. These deviations are connected to the underlying dependence of the thermal conductance with curvature.

Nanoparticles in the full wetting regime, F>0.25, feature a strong dependence of the thermal conductance on nanoparticle-solvent interaction strength. Such a dependence is consistent with experimental measurements of the thermal conductance of alkane monolayer-water planar interfaces. It was shown that the thermal conductance increases with the hydrophilicity, *i.e.*, the strength of the monolayer-water interactions [14]. Smaller internal energy transfer rates are expected when the liquid-solid interaction is weak, a notion that has been confirmed in several simulation studies [17,22,42,43]. Our results for the thermal conductance in the high solvent-nanoparticle interaction regime show that a similar principle applies to nanoparticle-fluid interfaces. Indeed, beyond the wetting transition, F>0.25, the thermal conductance increases significantly, by about 5-6 times for F$\sim$1, with values corresponding to the high end of thermal conductances ($\sim$ 250 MW/(K m^2)). These values are of the order of the ones found in experiments of AuPd nanoparticles ($\sim 4-22$ nm diameter) [44], which in our units would correspond to radii $R^* \sim 5-30$. Interestingly, it was concluded in that work that the thermal conductance is independent of the particle size. We will examine this question below.

In the full wetting regime we cannot use the correlation with the contact angle that we employed to construct Fig. 6. In order to shed light on the large increase of the thermal conductance with the solid-liquid interactions in this regime, we have computed the fluid density profiles around the nanoparticles. We show in Fig. 7 the density profiles for a partial wetting situation ($F = 0.1$) and two wetting states (F=0.5 and 1), for a nanoparticle of radius $R^* = 5$. Our results show large differences between the fluid structure in the partial wetting F=0.1 and full wetting F>0.25 regimes. At low interaction strengths the fluid develops a depletion layer around the nanoparticle and there is little evidence for adsorption on the nanoparticle surface. At high interaction strengths, F=0.5 and 1, the fluid develops a strong structure around the nanoparticle. The layering induced by the nanoparticle extends to long distances inside the bulk fluid, $r^* \sim 10$. The density profiles for these two states, F=0.5 and 1, feature a double adsorption peak ($r^* \sim 5, 5.7$) which is connected to the underlying faceted structure of our nanoparticle, which results in two characteristic radial distances for adsorption. The fluid particles adsorb strongly on the nanoparticle surface, which acts as a template for the adsorbed layer (see structure of the monolayer). Heat transfer across this interface is more favourable and this explains the strong increase of the thermal conductance with the nanoparticle-fluid interaction strength.

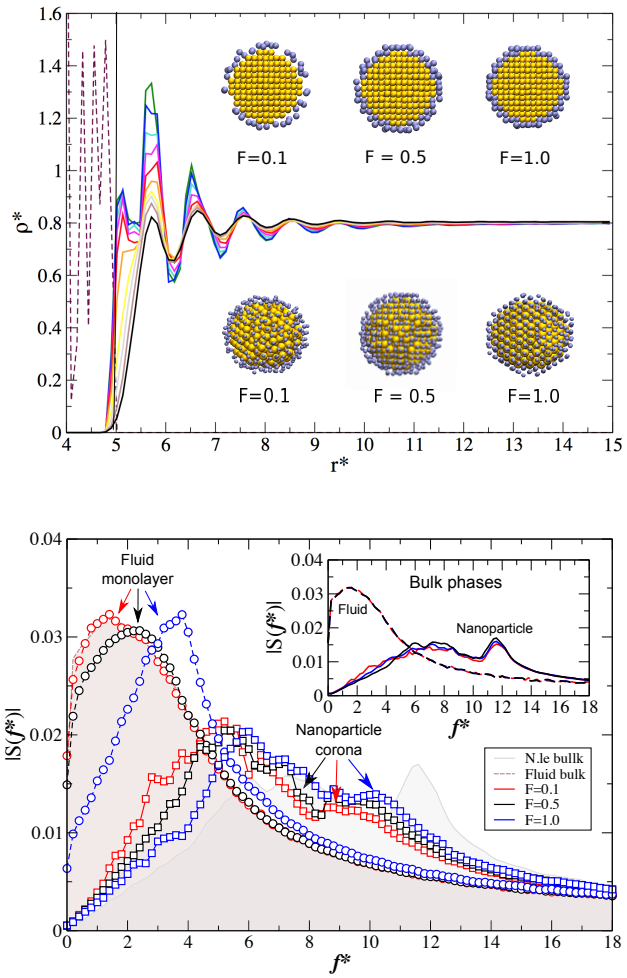

Fig. 7 (Top) Density profiles of the solvent around a nanoparticle of radius $R^* = 5$ (the vertical line indicates the particle radius) for partial wetting and wetting states. The different lines correspond to different solvent-particle interaction strengths. Focusing on the main peak $r^* \sim 6$ the lines correspond to, from bottom to top, F=0.05, 0.1, 0.15, 0.2, 0.3, 0.4, 0.5, 0.6, 0.8, 1. The snapshots show the structuring of the fluid around the nanoparticle for three representative interaction strengths. (Bottom) Density of states for nanoparticles with nanoparticle-fluid interactions corresponding to a partial wet state (F=0.1) and to wet states (F = 0.5, 1). The main panel shows the contributions from the atoms on the surface of the nanoparticle (squares), corresponding to the nanoparticle corona, and the fluid monolayer (circles) in direct contact with the nanoparticle. The "||" symbol refers to the amplitude of the Fourier transform and f^* is the frequency in Lennard-Jones units. The inset shows the contribution from the remaining particles, which correspond to the "bulk" nanoparticle and "bulk" fluid. The bulk contribution for the nanoparticle (grey area) and the fluid (brown area) are also shown in the main panel ("N.le" and "Fluid"), to facilitate the comparison with the interfacial contributions.

The structural changes discussed above must result in a distinctive modification of the dynamic properties of the fluid adsorbed on the nanoparticle surface and the nanoparticle atoms in direct contact with this fluid. The vibrational density of states has been considered before in theories of interfacial conductance [45], which focused on the density of states of the bulk phases in contact.

Computer simulation offers the possibility of splitting the interfacial and bulk contributions to the density of states. The density of states can be obtained from the power spectra of the velocity autocorrelation function (VAF):

$$\tilde{S}(\omega) = \int_0^{t_{max}} \left[\frac{VAF(t)}{VAF(0)}\right] \exp(i\omega t)dt, \quad (6)$$

where t_{max} is the maximum time used to compute the velocity autocorrelation function, which is obtained from

$$VAF(t) = \frac{1}{N_\alpha}\sum_{i=1}^{N_\alpha} \langle \mathbf{v}_i(t)\cdot\mathbf{v}_i(0)\rangle, \quad (7)$$

where N_α is the number of particles of type α, *i.e.*, nanoparticle, bulk fluid or interfacial fluid. To compute the interfacial contributions we defined a spherical shell around the nanoparticle and the fluid solvating layer (see ESI†). We show in Fig. 7-(bottom) the density of states (DoS) of the "bulk" and interfacial contributions. The DoS of the nanoparticle shows a structure similar to the phonon density of states of extended three dimensional solids[46]. Our results show that the DoS of the "bulk" phases, nanoparticle and fluid, are independent of the fluid-particle interaction, hence it is not possible to establish a direct correlation between these DoS and the thermal conductance. However the interfacial contribution to the DoS features a significant dependence, for both the surface atoms of the nanoparticle and the interfacial fluid. The DoS of the fluid shifts to higher frequencies, leading to a better overlap of the DoS of the nanoparticle and fluid atoms. This observation is consistent with an enhancement of the thermal conductance that is connected to a better vibrational coupling of the interfacial atoms.

We have focused our analysis on the impact of the nanoparticle-fluid interactions on the interfacial thermal conductance. We now discuss the dependence of the thermal conductance with particle size addressing the influence of the interfacial curvature on the thermal conductance. We show in Fig. 8 the variation of the thermal conductance with particle curvature (or particle size), and fluid-particle interaction strength. All the thermal conductances, irrespective of the interaction strength, decrease with decreasing curvature. This result is consistent with previous observations in oil-water interfaces (see ref.[18]), and in subsequent simulation work of oxide-alkane interfaces[19], as well as theoretical studies of droplets in coexistence with vapour[21]. The dependence of the thermal conductance of the nanoparticles can be fitted to the eqn

$$G_K\left(\frac{1}{R}\right) = G_K(0) + \frac{\delta}{R}, \quad (8)$$

where $G_K(0)$ is the thermal conductance of the corresponding flat surface, and δ quantifies the change of the thermal conductance with particle curvature. We find that $\delta > 0$ for all the cases investigated here, hence our simulations show that the curvature enhances the thermal conductance, in other words, highly curved interfaces are better thermal conductors. We have investigated the adsorption of fluid as a function of the particle size. The adsorption corresponding to the first fluid layer was estimated from

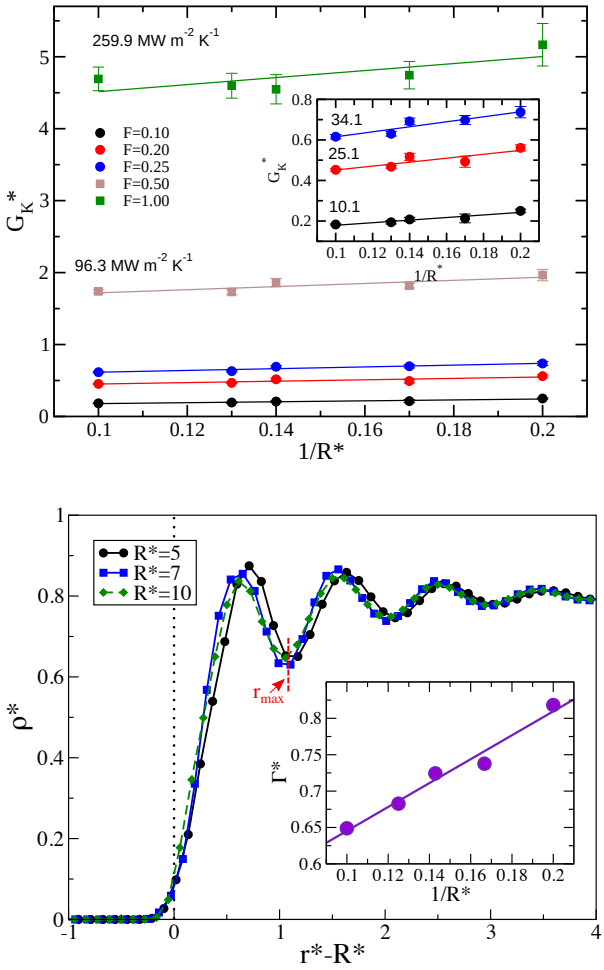

Fig. 8 (Top) Thermal conductance of the nanoparticles as a function of the particle curvature, $1/R^*$, and interactions strength, F. The numbers indicate the thermal conductance for $1/R^* = 0.1$ in SI units, using $\sigma = 3.405$ Å and $\varepsilon_f = 0.996$ kJ/mol as conversion factors for the effective diameter and interaction strength of the fluid. The inset shows the dependence of the thermal conductance in the partial-dry/wet states, 0.1 < F < 0.25. (Bottom) Density profiles of the fluid around nanoparticles of different radii and interaction strength F=0.1. The inset shows the dependence of the adsorption, Γ^* (see text and eqn (9) for details) with the curvature of the nanoparticle, $1/R^*$. The error associated to the data is of the order of the symbol size. r_{max} indicates the integration limit used in eqn (9).

$$\Gamma^* = N_l/A^* = R^{*-2}\int_0^{r_{max}} r^2\rho^*(r)dr, \quad (9)$$

where A^* represents the area of the nanoparticle or radius R^* and r_{max} is the distance at the first minimum in the density profile, $\rho^*(r)$, (see Fig. 8-(bottom), which shows the profiles for F=0.1 and several nanoparticle radii, $R^* = 5, 7, 10$). Interestingly, the adsorption decreases with decreasing curvature, approximately in a linear fashion, see inset in Fig. 8-(bottom). This result shows that curvature dependence of thermal conductance is correlated with the adsorption, or in other words, with the surface density

of the fluid layer in direct contact with the nanoparticle. This result thus provides a microscopic explanation of the curvature dependence in terms of the fluid-nanoparticle correlations.

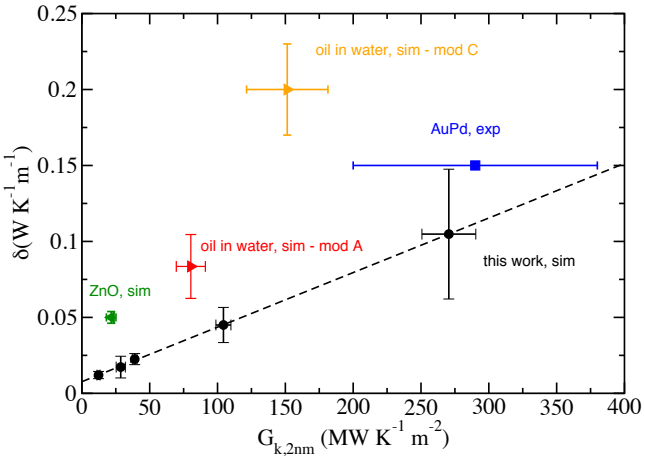

Fig. 9 Dependence of the parameter δ on the thermal conductance for nanoparticles of radius 2 nm. The circles and dashed line are results obtained with the model introduced in this work. The other symbols have the following meaning. Right triangle: simulation results for oil nanodroplets in water (taken from reference [18], "mod A" and "mod C" refer to the different models employed in that work). Left triangle: simulation results for ZnO nanoparticles in tetradecane (from reference [19]). Blue square: thioalkylated ethylene glycol-stabilized AuPd nanoparticles in water (from reference [44]).

We also find that the variation of the thermal conductance with curvature depends on the characteristic fluid-nanoparticle interactions. Stronger interactions (wet states) result in a stronger dependence (δ in eqn (8) increases). Following the linear dependence in eqn (8), it is possible to predict the thermal conductance of a flat surface from the thermal conductances of particles of varying sizes. The extrapolated conductances, $G_K(0)$, are reported in Table 1. We have tested the consistency of these predictions by performing additional computations of a fluid in contact with "flat surfaces" of varying interaction strengths, F. The thermal conductance, $G_k(0)$, was computed again from the temperature jump at the interface and the heat flux imposed in the non-equilibrium simulation. The results for the flat surfaces show very good agreement with the ones extrapolated from eqn (8) (see Table 1), and confirm the validity of this equation.

One aspect that remains to be discussed is how the dependence of the thermal conductance is expected to vary in experimental situations. Experimental studies of gold nanoparticles reveal a large range of thermal conductances depending on the chemical composition and the solvent employed. The thermal conductance of alkanethiol coated AuPd (3-5 nm diameter)-toluene interfaces is low, ~ 15 MW/(m^2 K), while in water is one order of magnitude higher [15,44], 250$\pm$90 (3-5 nm), 145$\pm$55 (3-5 nm) and 230$\pm$50 (22 nm), most likely connected to the hydrophilic character of the ligands. The values reported in our work cover this wide range of thermal conductances. For high G_K values, $\sim$200 MW/(m^2 K), our model predicts that the thermal conductance would increase by ~ 25 MW/(m^2 K) in decreasing the particle diameter from 22 nm to 3 nm. The analysis of the available data shows that current experimental data do not offer high sensitivity, which makes difficult to resolve the dependence with particle size with enough precision (see uncertainties in the thermal conductances quoted above). Nonetheless, some of the experimental data for nanoparticles can be compared with existing data for flat surfaces, where, according to our model, differences in thermal conductances are expected to be larger. The thermal conductance of AuPd particles stabilized with thioalkylated ethylene glycol is 250$\pm$90 MW/(m^2 K) [44].

Thermoreflectance experiments of polyethylene glycol silane monolayers on silver have shown that the thermal conductance is of the order of 180$\pm$30 MW/(m^2 K) [14]. Assuming the nanoparticle and flat thermal conductances for these systems are comparable, given the similar chemical composition of the ligands, one could estimate the curvature dependence of the thermal conductance. Using the experimental values for the flat interface and the nanoparticle (assuming $\sim$ 2 nm radius) we get $\delta = dG_K/d(1/R) \sim 0.15$ MW/(K m). This result is of the same order as the one we obtain for nanoparticles with large thermal conductances (see δ values in Table 1).

Computer simulations of nanoparticles have provided additional predictions of the thermal conductance. Recent simulations of small nanodroplets immersed in water predicted conductances of the order of $G_K \sim 100$ MW/ (m^2 K) for $1/R \sim 0.1$ nm^{-1} [18], which in our model would correspond to a medium interaction strength between the fluid and the particle. The coefficient determining the curvature dependence can be estimated from the simulation data to be of the order of $\delta \sim 0.2$ or 0.1 W/(K m) depending on the model employed in the analysis of the simulation data (See models A and C in reference [18]). Computer simulations of oxide zinc nanoparticles, ~ 2 nm, immersed in an alkane solvent predicted low thermal conductances, ~ 25 MW/(m^2 K) for $1/R \sim 0.15$ nm [19]. The curvature dependence that can be inferred from analysis of the results reported in ref. [19] is consistently lower, $\delta \sim 0.05$ W/(K m). These results for the curvature dependence are of the order predicted by our model.

We have collected in Fig. 9 the available simulation and experimental data showing the dependence of the variation of δ with the thermal conductance, using as a reference thermal conductances of 2 nm radius nanoparticles, for which both experimental and simulation estimates are available. Admittedly, the current experimental estimates involve significant uncertainties. The general trend, however, for both simulation and experiments is consistent with the predictions of our model. These data support our conclusion that higher thermal conductances involve stronger variations of the conductance with curvature.

4 Conclusions

Using molecular dynamics computer simulations and a generic model of a nanoparticle immersed in a fluid, we have investigated and quantified the dependence of the thermal conductance with both the nanoparticle size (interfacial curvature) and the nanoparticle-fluid interaction strength. Our work reveals a subtle interplay of nanoparticle size and interfacial interactions that defines the thermal conductance of nanoparticle interfaces over

F	$G_K^*(0)$	$G_K(0)$ (MW K^{-1} m^{-2})	δ (W K^{-1} m^{-1})	$G_{K,fs}$ (MW K^{-1} m^{-2})
0.1	0.114±0.025	6.25±1.12	0.0121±0.0024	9.33±0.48
0.2	0.370±0.069	20.01±3.39	0.0173±0.0072	
0.25	0.499±0.039	27.68±1.75	0.0225±0.0037	28.3±1.4
0.5	1.483±0.118	81.84±5.53	0.0450±0.0116	80.3±11.2
1.0	3.916±0.366	218.1±19.9	0.1048±0.0427	216.1±47.8

Table 1 Dependence of the thermal conductance with the nanoparticle-fluid interaction strength, F. $G_K(0)$ is the thermal conductance for a flat surface ($1/R = 0$) obtained from the extrapolation of the linear regression represented in Fig. 8-top and eqn (8) . The quantities with the $*$ denote reduced units. $\delta = dG_k/d(1/R)$ is the slope of the linear regressions represented in Fig. 8-top, and $G_{K,fs}$ is the thermal conductance obtained from computer simulations of flat surfaces in contact with the fluid.

a wide range of length scales, from small nanoparticles, 1 nm, to the flat interface limit.

For interaction strengths corresponding to the nanoparticle-fluid partial wetting regime we find a linear correlation between the thermal conductance and the free energy of adsorption of the nanoparticle. This result is of practical significance, since it connects the thermal conductance of nanoscale interfaces with an experimentally measurable property, the contact angle. Now it is possible to measure contact angles of truly small nanoparticles (few nanometers diameter) [29] using neutron probes, providing a route to estimate adsorption free energies. These recent advances may provide an approach to verify the correlations presented in our work.

Beyond the partial wetting regime, in the wetting region, the thermal conductance increases with the fluid-nanoparticle interaction strength. This observation can be rationalized in terms of the enhanced adsorption of the fluid on the nanoparticle surface, and the increased overlap in the vibrational density of states of the fluid layer adsorbed at the nanoparticle and the density of states of the nanoparticle surface.

We have shown that the thermal conductance increases with interfacial curvature for a wide range of fluid-nanoparticle interaction conditions. Generally, small nanoparticles are better heat conductors than larger ones. The curvature dependence of the thermal conductance can be fitted to a linear equation, $G_K(1/R) = G_K(0) + \delta/R$, which depends on the nanoparticle curvature, $1/R$, the thermal conductance in the limit of a flat surface, $G_K(0)$, and the parameter δ, which measures the "strength" of the curvature dependence. We found that large/strong thermal conductances/interactions lead to larger values of δ. We have tested these predictions against experiments of AuPd nanoparticles and simulations of oxide nanoparticles. This limited set of data follows the main predictions of our model. An analysis of our results indicates that the dependence of the thermal conductance on curvature is closely connected to the change in fluid adsorption with particle radius. For the same interaction strength, we find that small particles feature a stronger adsorption, namely, the surface density of the fluid layer in direct contact with the substrate is higher. This notion provides a microscopic explanation of the observed curvature dependence.

We expect that our work will motivate new experiments and simulations. The synergy between these two approaches should play an important role to quantify thermal conductances at the nanoscale and to address, experimentally, the dependence of the thermal conductance on particle size and composition. The connection of thermal conductance and nanoparticle wettability/adsorption may provide new routes to design experiments that exploit this correlation, and that may help to reduce the large level of uncertainty in the measurements obtained with current methods, based on optical absorption. Ultimately, a better understanding of heat transport at the nanoscale and its dependence on nanoparticle curvature will help to advance the use of nanoparticles in technological and medical applications.

5 Acknowledgements

We thank the EPSRC-UK (EP/J003859/1) for financial support. We acknowledge the Imperial College High Performance Computing Service for providing computational resources. We also acknowledge funding from the EU 7th Framework Programme ITN-SNAL, the NANO-BRIDGE (PRIN 2012, grant number 2012LHP-SJC), NANOSTEP (Fondazione CRT, Torino) and the MULTINANO (PRACE) projects.

References

1 X.-M. Lin, Y. Sun, E. V. Shevchenko, S. K. R. S. Sankaranarayanan, D. John, I. Fedin, F. Bresme, H. Mohwald, P. Moriarty, C. M. Sorensen and B. M. Law, *Chem. Commun.*, 2015, **51**, 13725–13730.

2 J. B. Edel, A. A. Kornyshev, A. R. Kucernak and M. Urbakh, *Chem. Soc. Rev.*, 2016, **45**, 1581–1596.

3 W. Lin, *Chemical Reviews*, 2015, **115**, 10407–10409.

4 J. Wilton-Ely, *Dalton Trans.*, 2008, 25–29.

5 S. M. Rogers, N. Dimitratos, W. Jones, M. Bowker, A. G. Kanaras, P. P. Wells, C. R. A. Catlow and S. F. Parker, *Phys. Chem. Chem. Phys.*, 2016, **18**, 17265–17271.

6 Z. Jiang, J. He, S. A. Deshmukh, P. Kanjanaboos, G. Kamath, Y. Wang, S. K. R. S. Sankaranarayanan, J. Wang, H. M. Jaeger and X.-M. Lin, *Nat. Mater.*, 2015, **14**, 912.

7 J. E. Reiner, J. W. F. Robertson, D. L. Burden, L. K. Burden, A. Balijepalli and J. J. Kasianowicz, *J. Am. Chem. Soc.*, 2013, **135**, 3087–3094.

8 C. Crick, P. Albella, B. Ng, A. Ivanov, T. Roschuk, M. Cecchini, F. Bresme, S. Maier and J. Edel, *Nano Lett.*, 2015, **15**, 553–559.

9 V. Kotaidis, C. Dahmen, G. von Plessen, F. Springer and A. Plech, *J. Chem. Phys.*, 2006, **124**, 184702.

10 D. Jaque, L. Martinez Maestro, B. del Rosal, P. Haro-Gonzalez, A. Benayas, J. L. Plaza, E. Martin Rodriguez and J. Gar-

cia Sole, *Nanoscale*, 2014, **6**, 9494–9530.

11 D. G. Cahill, P. V. Braun, G. Chen, D. R. Clarke, S. Fan, K. E. Goodson, P. Keblinski, W. P. King, G. D. Mahan, A. Majumdar, H. J. Maris, S. R. Phillpot, E. Pop and L. Shi, *App. Phys. Rev.*, 2014, **1**, 011305.

12 M. Hu, X. Wang, G. Hartland, V. Slagueirino-Maceira and L. Liz-Marzan, *Chem. Phys. Lett.*, 2003, **372**, 767–772.

13 E. Chiavazzo, M. Fasano, P. Asinari and P. Dacuzzi, *Nature Comm.*, 2014, **5**, 3565.

14 Z. Ge, D. Cahill and P. Braun, *Phys. Rev. Lett.*, 2006, **96**, 186101.

15 O. Wilson, X. Hu, D. Cahill and P. Braun, *Phys. Rev. B*, 2002, **66**, 224301.

16 H. Patel, S. Garde and P. Keblinski, *Nano Lett.*, 2005, **5**, 2225–2231.

17 N. Shenogina, R. Godawat, P. Keblinski and S. Garde, *Phys. Rev. Lett.*, 2009, **102**, 156101.

18 A. Lervik, F. Bresme and S. Kjelstrup, *Soft Matter*, 2009, **5**, 2407–2414.

19 M. Hu, D. Poulikakos, C. P. Grigoropoulos and H. Pan, *J. Chem. Phys.*, 2010, **132**, 164504.

20 O. Wilhelmsen, D. Bedeaux, S. Kjelstrup and D. Reguera, *J. Chem. Phys.*, 2014, **140**, 024704.

21 O. Wilhelmsen, D. Bedeaux and S. Kjesltrup, *Phys. Chem. Chem. Phys.*, 2014, **16**, 10573–10586.

22 L. Xue, P. Keblinski, S. R. Phillpot, S. U.-S. Choi and J. A. Eastman, *J. Chem. Phys.*, 2003, **118**, 337–339.

23 K. M. Stocker, S. M. Neidhart and J. D. Gezelter, *J. App. Phys.*, 2016, **119**, 025106.

24 S. Merabia and K. Termentzidis, *Phys. Rev. B*, 2012, **86**, 094303.

25 K. Issa and A. Mohamad, *Phys. Rev. E*, 2012, **85**, 031602.

26 S. Merabia, S. Shenogin, L. Joly, P. Keblinski and J.-L. Barrat, *Proc. Natl. Acad. Sci. USA*, 2009, **106**, 15113–15118.

27 E. A. Mastny and J. J. de Pablo, *J. Chem. Phys.*, 2007, **127**, 104504.

28 H. Heinz, R. A. Vaia, B. L. Farmer and R. R. Naik, *J. Phys. Chem. C*, 2008, **112**, 17281–17290.

29 J. Reguera, E. Ponomarev, T. Geue, F. Stellacci, F. Bresme and M. Moglianetti, *Nanoscale*, 2015, **7**, 5665–5673.

30 S. Plimpton, *J. Comp. Phys.*, 1995, **117**, 1 – 19.

31 A. Trokhymchuk and J. Alejandre, *J. Chem. Phys.*, 1999, **111**, 8510–8523.

32 F. P. Incropera, *Fundamentals of Heat and Mass Transfer*, John Wiley & Sons, 2006.

33 J. H. Irving and J. G. Kirkwood, *The Journal of Chemical Physics*, 1950, **18**, 817–829.

34 B. Hafskjold, T. Ikeshoji and S. Ratkje, *Mol. Phys.*, 1993, **80**, 1389–1412.

35 F. Bresme, B. Hafskjold and I. Wold, *J. Phys. Chem.*, 1996, **100**, 1879–1888.

36 J. Muscatello and F. Bresme, *J. Chem. Phys.*, 2011, **135**, 234111.

37 F. Bresme and M. Oettel, *J. Phys.: Conds. Matt.*, 2007, **19**, 41301.

38 H. Kaburaki, J. Li and S. Yip, *Mater. Res. Soc. Symp. Proc.*, 1999, **538**, 503–508.

39 J. Simon, S. Kjelstrup, D. Bedeaux and B. Hafskjold, *J. Phys. Chem. B*, 2004, **108**, 7186.

40 F. Bresme and N. Quirke, *Phys. Rev. Lett.*, 1998, **80**, 3791–3794.

41 R. Aveyard and J. H. Clint, *J. Chem. Soc., Faraday Trans.*, 1996, **92**, 85–89.

42 J.-L. Barrat and F. Chiaruttini, *Mol. Phys.*, 2003, **101**, 1605–1610.

43 A. Giri and P. E. Hopkins, *App. Phys. Lett.*, 2014, **105**, 033106.

44 Z. Ge, D. G. Cahill and P. V. Braun, *J. Phys. Chem. B*, 2004, **108**, 18870–18875.

45 E. T. Swartz and R. O. Pohl, *Rev. Mod. Phys.*, 1989, **61**, 605–668.

46 P. Heino, *Phys. Rev. B*, 2005, **71**, 144302.